

Flares from plasmoids and current sheets around Sgr A*

I. Dimitropoulos^{*1,2}, A. Nathanail^{**2}, M. Petropoulou^{3,4}, I. Contopoulos², C. M. Fromm^{5,6,7}

¹ Department of Physics, University of Patras, Rio 26504, Greece

² Research Center for Astronomy and Applied Mathematics, Academy of Athens, Athens 11527, Greece

³ Department of Physics, National and Kapodistrian University of Athens, University Campus Zografos, GR 15784, Athens, Greece

⁴ Institute of Accelerating Systems & Applications, University Campus Zografos, GR 15784, Athens, Greece

⁵ Institut für Theoretische Physik und Astrophysik, Universität Würzburg, Emil-Fischer-Strasse 31, 97074 Würzburg, Germany

⁶ Institut für Theoretische Physik, Goethe Universität Frankfurt, Max-von-Laue-Str.1, 60438 Frankfurt am Main, Germany

⁷ Max-Planck-Institut für Radioastronomie, Auf dem Hügel 69, D-53121 Bonn, Germany

September 11, 2024

ABSTRACT

Context. The supermassive black hole Sgr A* at the center of our galaxy produces repeating near-infrared flares that are observed by ground and space based instruments. This activity has been simulated in the past with Magnetically Arrested Disk (MAD) models which include stable jet formations. The present study uses a different approach in that it considers a Standard and Normal Evolution (SANE) multi-loop model that lacks a stable jet structure.

Aims. The main objective of this research is to identify regions that contain current sheets and high magnetic turbulence, and to subsequently generate a 2.2 μm light curve generated from non-thermal particles. These aims require the identification of areas which contain current sheets and high magnetic turbulence, and the averaging of the magnetization in the regions surrounding these areas. Subsequently, Particle-in-Cell (PIC) fitting formulas are applied to determine the non-thermal particle distribution and to obtain the sought after light curve. Additionally, we investigate the properties of the flares, in particular, their evolution during flare events, and the similarity of flare characteristics between the generated and observed light curves.

Methods. 2D GRMHD simulation data from a SANE multi-loop model is employed, and thermal radiation is introduced to generate a 230 GHz light curve. Physical variables are calibrated to align with the 230 GHz observations. Current sheets are identified by analyzing toroidal currents, magnetization, plasma β , density, and dimensionless temperatures. The evolution of current sheets during flare events is studied, and higher-energy non-thermal light curves are calculated, focusing on the 2.2 μm near-infrared range.

Results. We obtain promising 2.2 μm lightcurves whose flare duration and spectral index behavior align well with observations. Our findings support the association of flares with particle acceleration and nonthermal emission in current sheet plasmoid chains and in the boundary of the disk inside the funnel above and below the central black hole.

Key words. black hole physics – GRMHD - Sgr A* - current sheets - magnetic reconnection - NIR flares

1. Introduction

In the center of the Milky Way at a distance of $D \simeq 8.3$ kpc lies Sagittarius A* (Sgr A*), a $4.2 \times 10^6 M_{\odot}$ supermassive black hole (hereafter SMBH; GRAVITY Collaboration et al. 2022). The accretion disk around it is optically thin, with collisionless high-temperature low-density plasma. Its bolometric luminosity is in the sub-Eddington range of $L \sim 10^{36}$ erg s⁻¹ (Genzel et al. 2010). The emission from Sgr A* is systematically monitored over a very wide range of frequencies, allowing us to investigate the dynamics of the disk in the vicinity of a SMBH.

Observations from the GRAVITY Collaboration have shown a hot spot rotating around Sgr A* with a period of ~ 60 minutes at a distance of a few gravitational radii (hereafter r_g) from the black hole (GRAVITY Collaboration et al. 2018). Sgr A* is known to exhibit variability in the near infrared which manifests itself in the form of several flares over a single day (Ghez et al. 2005a; Do et al. 2019). For the first time, GRAVITY observations revealed that a flare in Sgr A* coincided with a hot spot moving around the central black hole. Several investigations suggest that flares originate in highly magnetized structures

that are formed in the innermost region of the black hole and produce synchrotron radiation (Dodds-Eden et al. 2009; Boehle et al. 2016; Ponti et al. 2017; Chatterjee et al. 2021; Scepi et al. 2022).

Analytical models have been applied to study the trajectory of the hot spots in the resulting lightcurve and showed the importance of the effect of gravitational lensing (GRAVITY Collaboration & Loeb 2005; Younsi & Wu 2015; Bauböck et al. 2020; Ball et al. 2021). As shown by Matsumoto et al. (2020), assuming that its motion is in the equatorial plane, the GRAVITY hot spot follows a circular path at super-Keplerian velocity. However, an outflowing conical sub-Keplerian orbit can fit these observations equally well (Antonopoulou & Nathanail 2024).

Lately, the theoretical astrophysics community has increasingly turned to numerical simulations, specifically to general relativistic magnetohydrodynamic simulations (hereafter GRMHD), in order to gain a comprehensive understanding of the dynamics involved in accreting black holes. Observations of flares and moving hot spots further emphasizes the significance of considering both magnetic fields and fluid dynamics within the extreme gravitational environment near a black hole (Dexter et al. 2020; Porth et al. 2021; Chatterjee et al. 2021; Čemeljić

* up1098378@upatras.gr

** anathanail@academyofathens.gr

et al. 2022; Scepi et al. 2022; Mellah et al. 2023; Lin & Yuan 2024).

Numerical investigations explore the formation of current sheets in the vicinity of a black hole and the subsequent production of plasmoids and plasmoid chains (Nathanail et al. 2020; Nathanail et al. 2022; Ripperda et al. 2022). Current sheets are responsible for particle acceleration and the generation of variable non-thermal radiation. These models need to be supported by numerical studies of turbulence and magnetic reconnection in collisionless plasmas that self-consistently capture the dynamical interplay between particles and fields on the kinetic plasma scales. Such investigation can be performed with Particle-in-Cell (PIC) simulations (Drake et al. 2012; Guo et al. 2014; 2015; Sironi & Spitkovsky 2014; Shay et al. 2014; Dahlin et al. 2014; Li et al. 2015; 2023; Petropoulou & Sironi 2018; Werner et al. 2018; Ball et al. 2018; Comisso & Sironi 2019). In particular, these investigations help us study the acceleration processes in detail by tracking individual particles, but also characterize the properties of the particle distribution function, e.g. shape of distribution (power law, log-parabolic), fraction of energy carried by non-thermal particles, maximum particle energy and others (e.g., Werner et al. 2018; Ball et al. 2018; Petropoulou et al. 2019; Zhang et al. 2023). Some of the particle properties, like the slope of the power-law distribution, can be related, through empirical expressions, to the local plasma properties, such as magnetization $\sigma := B^2/\rho$ (where B is the magnetic field strength and ρ is the density) and plasma $\beta := 2P/B^2$ (where P is the pressure). These prescriptions can then be combined with GRMHD simulations to anticipate the generation of non-thermal, high-energy electron distributions with properties depending on the local physical conditions (Chatterjee et al. 2021; Scepi et al. 2022; Aimar et al. 2023; Lin et al. 2023; Mellah et al. 2023). The way to connect GRMHD simulations and PIC results is the following: after the plasma accretion process has reached an inflow equilibrium (Dexter et al. 2020), the thermal radiation is attributed to the hot electrons with a parameterized temperature derived from the simulation ion temperature (Mościbrodzka et al. 2016). In order to include non-thermal electrons to radiate, formulas from PIC simulations are employed. Non-thermal electron distributions are assumed in each cell depending on magnetization (for $\sigma < 5$) and plasma β (Davelaar et al. 2019; Fromm et al. 2022; Cruz-Orsorio et al. 2022). This study proposes a novel approach for incorporating non-thermal particles into simulation results. Specifically, current sheets are first identified (see also Vos et al. 2024), followed by characterizing their environment in terms of averaged quantities of magnetization σ and plasma β . Finally, non-thermal particles are sourced from the plasma within the current sheet. In this paper, we utilize the 2D GRMHD simulations of Nathanail et al. (2020) to investigate the ability of the current sheet and plasmoids to produce the observed non-thermal flaring activity of Sgr A*. A radiation model is applied to produce lightcurves at 230 GHz (thermal radiation from the disk) and 2.2 μm (non-thermal radiation from current sheets; see also Scepi et al. 2022). The structure of the paper is as follows: Section 2 describes the methodology of our investigation divided in three subsections in which we introduce the GRMHD simulation setup (2.1), the modeling of the radiation (2.2), and the method with which we determine current sheets and their environment from the GRMHD simulation (2.3). In Section 3 we present our results for the thermal (3.1) and non-thermal radiation (3.2). Finally, in Section 4 we present our conclusions and discuss prospects for future work.

2. Numerical setup

The numerical methods employed for the GRMHD simulation in this study closely mirror those used in previous research (Nathanail et al. 2020). We initialize the simulation with magnetic field configurations designed to generate multiple current sheets as the accretion system evolves. The formation of current sheets occurs in the vicinity of the black hole, and their subsequent reconnection gives rise to the development of multiple plasmoids and plasmoid chains. In order to assess the radiation characteristics of the current sheets formed and the subsequent generation of plasmoids, we employ a radiation proxy model. This model enables the calculation of both thermal and non-thermal radiation at 230 GHz and 2.2 μm , respectively.

2.1. GRMHD simulation

The accretion disk surrounding a black hole can be conceptualized as a hydrodynamic system in the context of curved spacetime, where the magnetic field significantly influences its dynamics. A GRMHD code integrates these physical properties into a unified numerical simulation and allows a robust evolution in time where the accretion and accumulation of magnetic flux produce energetic phenomena. We employ the BHAC code (Porth et al. 2017) which solves the ideal MHD equations in general relativity, namely

$$\nabla_\mu(\rho u^\mu) = 0 \quad (1)$$

$$\nabla_\mu T^{\mu\nu} = 0 \quad (2)$$

$$\nabla_\mu *F^{\mu\nu} = 0 \quad (3)$$

where $T^{\mu\nu}$ and $*F^{\mu\nu}$ are the energy momentum tensor and the dual of the Faraday tensor, respectively. Here, we denote with ρ the rest-mass density and with u^μ the fluid four-velocity. Some important characteristics of the code are the following: it implements second-order high-resolution shock-capturing finite-volume methods and adaptive mesh-refinement (AMR) wherever needed. It also implements constrained-transport (Del Zanna et al. 2007) to guarantee a divergence-free magnetic field (Olivares et al. 2019).

Furthermore, the model is axisymmetric (2D), and the coordinates of the initial torus-like plasma distribution are spherical ($r \times \theta \times \phi$). We used a logarithmic radial grid and the domain extends out to 2500 r_g . The resolution of the model is $4096 \times 2048 \times 1$ cells. The torus at the initial equilibrium state has constant specific angular momentum $l = 4.28$ (Fishbone & Moncrief 1976). The inner radius was set to $r_{in} = 6 r_g$ and the pressure maximum radius to $r_{max} = 12 r_g$. All quantities are calculated in geometrized units ($G = c = 1$) in which the gravitational radius is equal to $r_g = M$. We considered a Kerr black hole with dimensionless spin $a = J/M^2 = 0.93$, where J and M are the angular momentum and mass of the black hole respectively. The radius of the event horizon is $r_h = 1.341 r_g$, and there are 29 grid cells inside the horizon.

The initial conditions for the magnetic field inside the torus consists of several loops of interchangeable clockwise-anticlockwise orientation between neighboring loops (see Fig. 1). In order to generate a magnetic field topology as described above we used a vector potential A_ϕ :

$$A_\phi \propto A \times B, \quad (4)$$

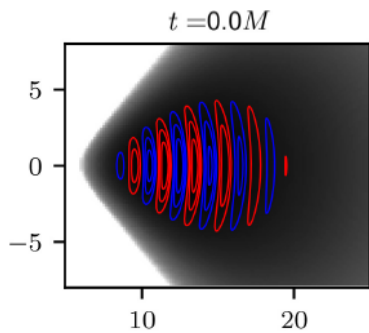


Fig. 1. Initial magnetic field (lines) and density (color) configuration in the initial torus. Axis coordinates calculated in r_g . Red and blue colors denote clockwise and anticlockwise direction of the magnetic field.

with

$$A \equiv \max(\rho/\rho_{max} - 0.2, 0), \quad (5)$$

$$B \equiv \cos[(N-1)\theta] \sin[2\pi(r-r_{in})/\lambda_r], \quad (6)$$

where N is the number of poloidal loops and λ_r their characteristic length scale, and ρ_{max} is the maximum rest mass density of the disk.

The above model is characterized as SANE multi-loop and has important differences from a classic Magnetically Arrested Disk (MAD) model. In a classic MAD there is a steady jet, whereas in the SANE multi-loop model no steady polar outflow develops. We have not yet observed a jet from Sgr A* and it is an open question in which direction our models should go for the interpretation of phenomena near the black hole. As discussed in Nathanail et al. (2022), images at 43 and 86 GHz will produce an extended stable jet base in the case of MAD model, whereas in the case of the SANE multi-loop model, the images will possibly have an extended jet-like structure only in the flaring state. We expect that new images of the Sgr A* black hole will further clarify the landscape of pertinent models.

2.2. Radiation model

In this subsection we discuss and present in detail the model that we used for the thermal and non-thermal radiation expected from plasma in the accretion flow. We employ an approximate "proxy" model for radiation which integrates the thermal emissivity across the entire disk. The validity of this method has been tested in the past against General Relativistic Radiative Transfer (hereafter GRRT) calculations (Porth et al. 2019). These comparisons demonstrated a close correspondence between the proxy method's results, the detailed GRRT calculations, and the observed variability in the lightcurve. Scepi et al. (2022) employed a similar strategy to investigate flares originating from current sheets and plasmoids for MAD models.

The total luminosity L_ν emitted by the fluid at a specific frequency ν (in units of ergs per second per Hz), is calculated based on the following equation:

$$L_\nu = \int_0^{2\pi} \int_0^\pi \int_{r_h}^{r_{max}} e^{-\tau_\nu} \times j_\nu(B, p, \rho) \times g_{redshift}^3 \sqrt{-g} d\phi d\theta dr \quad (7)$$

where j_ν is the emissivity of thermal or non-thermal processes at a specific frequency¹ and τ_ν is the opacity of the fluid to a given process at frequency ν . The terms $\sqrt{-g} d\phi d\theta dr$ represents the infinitesimal volume element dV for each grid point. Close to the black hole radiation in specific is suppressed by the gravitational redshift term ($g_{redshift}^3$; Viergutz 1993), where $g_{redshift} = \sqrt{\Sigma\Delta/A}$. Here, $A = (r^2 + a^2)^2 - a^2\Delta \sin^2\theta$, $\Sigma = r^2 + a^2 \cos^2\theta$ and $\Delta = r^2 - 2rM + a^2$. The parameter a corresponds to the spin of the BH, while M represents its mass, which is fixed at 1 in these forms (an estimation of $g_{redshift}$ for $r = 2r_g$, $\theta = \pi/4$ and $a = 0.93$ is approximately on the order of 10^{-1}). The observable radiation flux is given by $F_\nu = L_\nu/4\pi D^2$, where the distance from the black hole is $D = 8.277$ kpc (GRAVITY Collaboration et al. 2022). The integration of the luminosity works best when the viewing angle is nearly face on, as we are not taking into account the effects of Doppler beaming and gravitational lensing. The difference of such a method compared with a full GRRT calculation is of order unity (Scepi et al. 2022).

At 230 GHz, the thermal electron synchrotron radiation comes predominantly from the disk region, namely $\pi/3 \lesssim \theta \lesssim 2\pi/3$. In order to calculate the synchrotron emission of a thermal distribution of plasma, we utilize the formula developed by Leung et al. (2011) (see also Pandya et al. 2016). At 230 GHz, the emissivity of a fluid element in the disk is given by the equation

$$j_\nu = n_e \frac{\sqrt{2}\pi e^2 v_s}{6\Theta_e^{-2} c} X e^{-X^{1/3}} \quad (8)$$

n_e is the electron number density and $X \equiv \nu/\nu_s$, where $\nu_s \equiv (2/9)\nu_L \Theta_e^2 \sin\lambda$ (λ is the particle pitch angle with respect to the direction of the magnetic field), and $\nu_L \equiv eB/(2\pi m_e c)$ is the Larmor frequency. We use Θ_e to denote the dimensionless temperature of the electrons defined as

$$\Theta_e = \frac{m_p T_e P}{m_e T_p \rho} \quad (9)$$

where m_p, m_e are the masses of the proton and electron respectively, it is important to mention that the composition of the fluid is assumed to be electron-proton plasma. The ratio T_p/T_e is calculated from the prescription of Mościbrodzka et al. (2016) which describes the electron-to-proton coupling in low (disk) and high magnetized regions (funnel), namely

$$\frac{T_p}{T_e} = R_{high} \frac{\beta^2}{1 + \beta^2} + R_{low} \frac{1}{1 + \beta^2}, \quad (10)$$

where R_{high} and R_{low} are free parameters that determine the heating ratio of electrons. In our calculations we set $R_{high} = 20$ and $R_{low} = 1$, since we do not focus on a large parametric investigation of flares from such configurations. In Dihingia et al. (2023b), a comparison was made regarding the prescription of temperature ratios proposed by various studies (Mościbrodzka et al. 2016; Dihingia et al. 2023a; Meringolo et al. 2023). The results indicate that the model presented by Mościbrodzka et al. (2016) offers the most accurate approximation of temperature ratios within the disk region. The electron temperature in a

¹ There seems to be some confusion in the literature in the definition of 'emissivity'. Emissivity usually expresses the effectiveness of the surface of a material in emitting energy as thermal radiation. In the recent astrophysical literature, however, emissivity j_ν is defined as the energy loss per unit time per frequency per unit volume (e.g. Leung et al. 2011; Ghisellini 2013; Scepi et al. 2022). Note that Rybicki & Lightman 1986 define j_ν as the 'emission coefficient', i.e. the energy loss per unit time per frequency per unit volume per steradian.

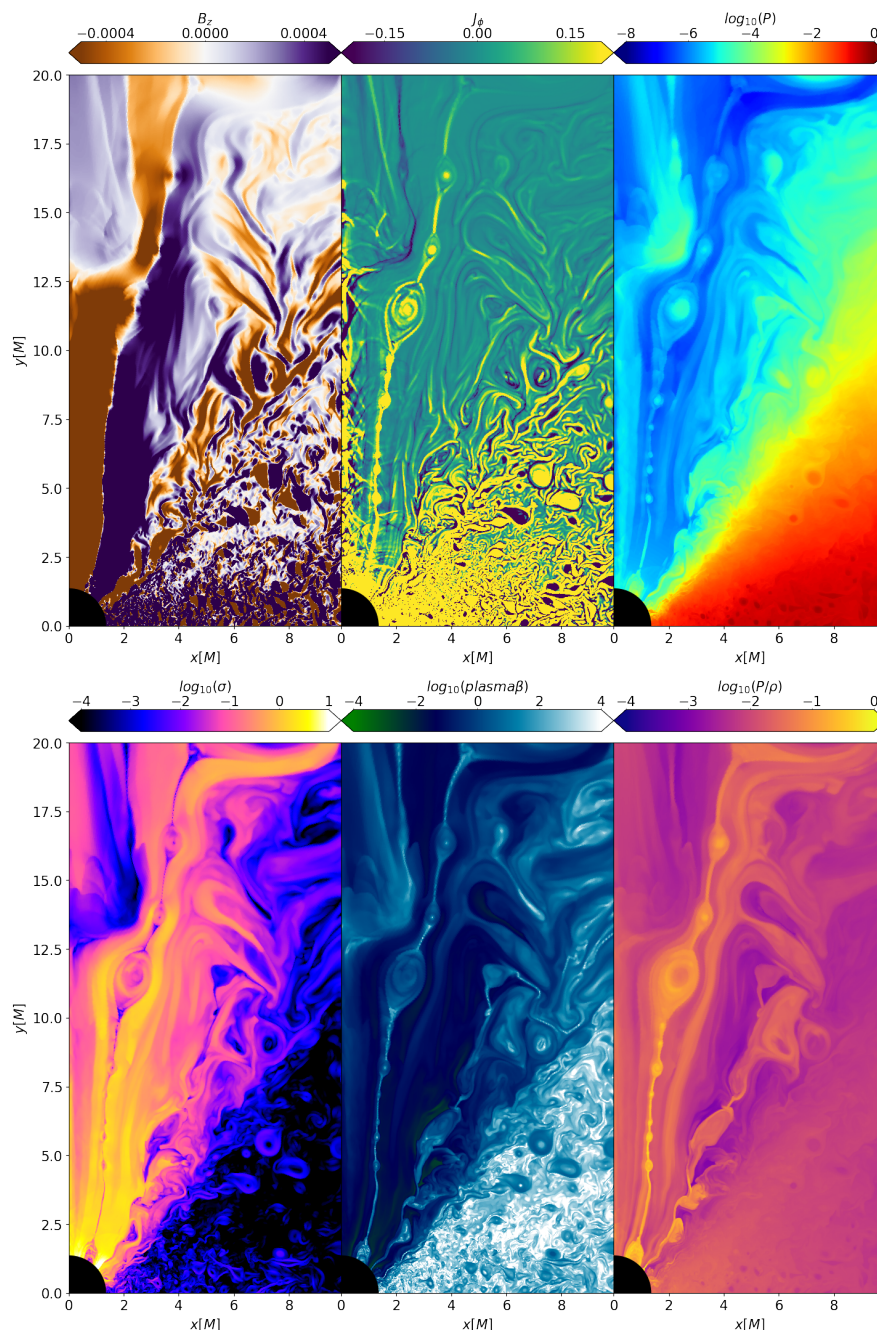


Fig. 2. Upper panel (from left to right): magnetic field B_z component, toroidal current and density. Lower panel (from left to right): magnetization, plasma β and dimensionless temperature Θ_p . By setting limits in these parameters, we define the red regions in Fig. 3.

GRMHD simulation can be determined through two temperature simulations that independently evolve this quantity (Jiang et al. 2023). Such studies highlight the importance of self-consistently evolving the electron temperature to accurately explore the thermal synchrotron radiation (Jiang et al. 2024).

The thermal radiation absorption term $e^{-\tau_\nu}$ is important only inside the disk. The optical depth is defined as $\tau_\nu = \int_{\pi/3}^{\theta_0} a_{\nu,th} ds$ where $ds = \sqrt{g_{\theta\theta}} d\theta$ ($\pi/3 \leq \theta_0 \leq 2\pi/3$ are the latitudinal limits of the disk). In the case of local thermal equilibrium, the source function of the emitting material is given by the Planck function B_ν . Then, the absorption coefficient of the material can be expressed as

$$a_{\nu,th} = j_\nu / B_\nu, \quad (11)$$

where

$$B_\nu = (2h\nu^3/c^2)[\exp(h\nu/kT_e) - 1]^{-1} \quad (12)$$

is the Planck function. So, the total luminosity for thermal radiation at each grid point (r_0, θ_0) is calculated as follows: First, we determine the emissivity at the point. Next, we compute the absorption term at all grid points (r, θ) where $r = r_0$ and $\pi/3 \leq \theta \leq \theta_0$. The sum of absorption coefficients ($a_{\nu,th}$) at these points provides us with the value of the optical depth τ_ν at (r_0, θ_0) . In this way, it is like integrating along light rays perpendicular to the equatorial plane.

The non-thermal emissivity at $2.2 \mu\text{m}$, which is attributed to the synchrotron radiation of relativistic electrons, is given by

(Rybicki & Lightman 1986, Ghisellini 2013)²

$$j_\nu = \frac{3\sigma_T c K U_B}{16\pi \sqrt{\pi} \nu_L} \left(\frac{\nu}{\nu_L} \right)^{-\frac{p-1}{2}} \quad (13)$$

where $U_B = B^2/(8\pi)$ is the energy density of the magnetic field. One needs also to determine the non-thermal electron distribution $n(\gamma) = K\gamma^{-p}$, so K is the electron number density multiplied by the efficiency ϵ of the radiation mechanism, and p is the slope of the distribution.

In the case of non-thermal radiation the integration of Eq. (7) is performed along the radial direction. In the funnel region (see e.g. colored region in Fig. 3), this is like integrating along rays perpendicular to the equatorial plane. The optical depth in this case is $\tau_\nu = \int_r^{r_{max}} a_{\nu, nth} ds$ where $ds = \sqrt{g_{rr}} dr$. $a_{\nu, nth}$ is the dimensionless absorptivity which for the non-thermal process is defined as

$$a_{\nu, nth} = \frac{\sqrt{\pi} e^2 K}{8m_e c} \nu_L^{\frac{p+2}{2}} \nu^{-\frac{p+4}{2}} f_a(p) \quad (14)$$

(Ghisellini 2013; Pandya et al. 2016), where the function $f_a(p)$ is a product of Γ functions, approximated by

$$f_a(p) \sim 3^{\frac{p+1}{2}} \left(\frac{1.8}{p^{0.7}} + \frac{p^2}{40} \right), \quad (15)$$

also in this case, the total luminosity for non-thermal radiation at each grid point is calculated as follows: First, we determine the emissivity at the point (r_0, θ_0) . Next, we compute the absorption term at all grid points (r, θ) where $r_0 \leq r \leq r_{max}$ and $\theta = \theta_0$. The sum of absorption coefficients ($a_{\nu, nth}$) at these points provides us with the value of the optical depth τ_ν at (r_0, θ_0) .

A GRMHD simulation does not have the necessary microphysics to follow the acceleration of particles and extract the electron distribution function or the efficiency for microscopic processes occurring within the plasma. In order to incorporate how energy is transferred from the magnetic field to the plasma, we used two different post-processing formulas from results of PIC simulations. The first approach is from a local investigation of idealized current sheets (Ball et al. 2018). The second one is from an investigation of microphysical properties of special-relativistic turbulence (Meringolo et al. 2023). The first approach was applied to the current sheets in the funnel region above the disk boundary, and the second one in the vicinity of the disk boundary. The results of such local investigations give us the opportunity to approximate the properties of the accelerated particles that will eventually radiate through the local plasma characteristics. Let us first define the non-thermal acceleration efficiency ϵ as the fraction of the kinetic energy carried by the non-thermal particles to the kinetic energy of the total electron population,

$$\epsilon = \frac{\int_{\gamma_{pc}}^{\infty} (\gamma - 1) \left[\frac{dN}{d\gamma} - f_{MB}(\gamma, \Theta_e) \right] d\gamma}{\int_{\gamma_{pc}}^{\infty} (\gamma - 1) \frac{dN}{d\gamma} d\gamma}, \quad (16)$$

where γ_{pc} denotes the peak of the spectrum and f_{MB} is a relativistic Maxwellian fitting function.

² The approximation by Ghisellini 2013 assumes that the min electron Lorentz factor is one and the maximum electron Lorentz factor is infinite. This implies that there is no high energy cut off in the emissivities, i.e. the spectral slope is the same at high energies. This is not 100% correct, and as a consequence, we are overestimating the high energy fluxes which includes the NIR, and certainly the X-rays.

According to Ball et al. (2018), Eq. (17) gives us the slope of the spectrum with respect to the magnetization σ and plasma β .

$$p = A_p + B_p \tanh(C_p \beta) \quad (17)$$

where $A_p = 1.8 + 0.7/\sqrt{\sigma}$, $B_p = 3.7\sigma^{-0.19}$, and $C_p = 23.4\sigma^{0.26}$. Moreover, the electron non-thermal efficiency with respect to the magnetization (σ) and plasma β is

$$\epsilon = A_\epsilon + B_\epsilon \tanh(C_\epsilon \beta), \quad (18)$$

where $A_\epsilon = 1 - 1/(4.2\sigma^{0.55} + 1)$, $B_\epsilon = 0.64\sigma^{0.07}$, and $C_\epsilon = -68\sigma^{0.13}$. On the other hand Eq. (19) approximates the slope p (for Eq. (19) it holds that $p = k - 1$) with respect to the same parameters based on Meringolo et al. (2023).

$$k = k_0 + \frac{k_1}{\sqrt{\sigma}} + k_2 \sigma^{-6/10} \tanh(k_3 \beta \sigma^{1/3}), \quad (19)$$

where $k_0 = 2.8$, $k_1 = 0.2$, $k_2 = 1.6$, and $k_3 = 2.25$. The efficiency of particle acceleration in turbulent plasmas is equal to

$$\epsilon = e_0 + \frac{e_1}{\sqrt{\sigma}} + e_2 \sigma^{0.1} \tanh[e_3 \beta \sigma^{0.1}], \quad (20)$$

where $e_0 = 1$, $e_1 = -0.23$, $e_2 = 0.5$ and $e_3 = -10.18$.

In the upcoming section 2.3, we will elaborate on how we determine current sheets and their associated parameters, such as magnetization and plasma β in their vicinity. The reason we are interested in the latter is because dissipative current sheets are fed with plasma from their environment. These conditions determine the strength of the non-ideal electric fields that accelerate particles and the rate of energy dissipation. All empirical relations that describe properties of the accelerated particle populations refer to the σ and plasma β parameters in the upstream regions of the current sheets. Once these areas of interest are identified, these formulas can then be applied to determine the slope of the distribution of accelerated electrons within the current sheets or turbulent regions at the disk boundary.

2.3. Determination of current sheets and their environment

PIC simulations that investigate current sheets start with a specific magnetization, a specific plasma β and an initial current layer in the middle. As the magnetic field evolves magnetic reconnection events take place, magnetic energy is dissipated, and particles are accelerated from the thermal pool to higher energies. Eqs. (17) and (19) are fitting models of the results of such PIC simulations which can give us the slope of the spectrum of the non-thermal electrons as functions of GRMHD quantities. It is important to emphasize that the parameter values that must be used in these formulas are roughly those set as initial conditions in a PIC simulation. As it turns out, these values are maintained during the calculation only in the environment surrounding the current sheets.

So, in order to use eqs. (17) and (19) it is necessary to constrain the current sheet and its surrounding environment. First, it is useful to distinguish the regions where current sheets form from the polarity reversal of the magnetic fields (Fig. 2, reversal of B_z). We utilize five variables to determine the current sheets, which are as follows: toroidal current $J_\phi := (\nabla \times B)_\phi$, density ρ , magnetization σ , plasma β and dimensionless temperature Θ_p (normalized to mc^2 which is equal with P/ρ). The remaining plots in Fig. 2 provide limits for each parameter that defines the exact region where a current sheet occurs. As we see in Fig. 2, a current sheet is characterized by high values of toroidal current,

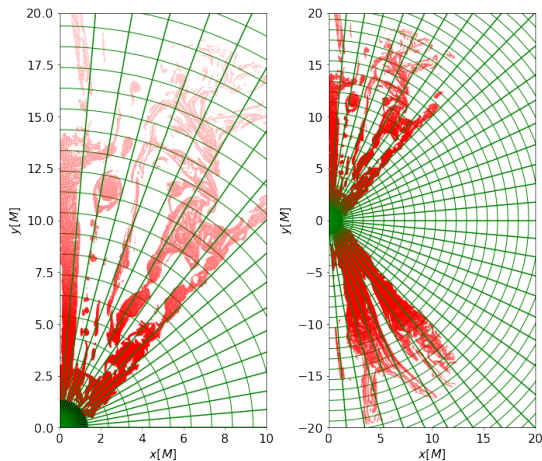


Fig. 3. Determination of plasma (red color) in the reconnection region and places of high magnetic turbulence. They are selected after applying limits on toroidal current, magnetization, plasma β , density and dimensionless temperature. The green grid corresponds to the discretization for the purpose of parameter averaging. Same snapshot as in Fig 2.

high values of density, low values of magnetization, high values of plasma β and high values of dimensionless temperature. Thus, we set the following limits for each parameter: $|J_\phi| > 10^{-4}$, a density floor (cutoff) at $\rho_{cut} = 2 \times 10^{-5}$, a magnetization ceiling cutoff at $\sigma_{cut} = 10$, a plasma β floor at $\beta_{cut} = 10^{-3}$ and finally a temperature floor at $\Theta_p = 10^{-3}$. By combining these constraints, we obtain the red regions in Fig. 3 which are clearly associated with the current sheets we identified. Additionally, the plasma in these red-colored regions has undergone the reconnection process. Efficient particle acceleration occurs in regions with high magnetization and low plasma β Ball et al. 2018. Such regions develop only in the funnel region, so we applied the above methodology exclusively to the plasma within this region.

Following this procedure we have identified the current sheets developed in the simulation. The next step involves characterizing the current sheet environment in terms of averaged quantities in order to use Eq. (17) and (19) for the plasma within the current sheet. To achieve this, a discretization method is employed, wherein the region is divided into cells with a radial length of $1 r_g$ and a meridional extent of 10 degrees in the θ direction. In each cell that contains part of a current sheet (red region) we calculate the mean values of magnetization σ and plasma β of their environment (white region) over 2 cells to the right and 2 to the left in the θ direction, namely

$$\bar{\sigma} = \frac{1}{4} \sum_{cell=-2}^{cell=+2} \sigma \quad (21)$$

$$\bar{\beta} = \frac{1}{4} \sum_{cell=-2}^{cell=+2} \beta \quad (22)$$

Subsequently, the slope of the non-thermal electrons inside the current sheet or in the turbulent plasma in each cell is computed using equations Eq. (17) and (19) with parameters values as $\sigma = \bar{\sigma}$ and $\beta = \bar{\beta}$. The plasma assumed to be accelerated corresponds to the region depicted in red in Fig. 3.

3. Results

In the next two subsections, we present our results on the thermal and non-thermal radiation. The first part covers calculations

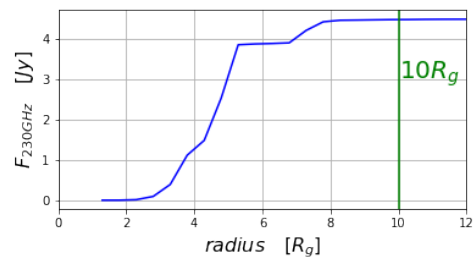


Fig. 4. Cumulative 230 GHz flux from all angles θ for radii less than or equal to r .

at 230 GHz (thermal component), which help calibrate the physical parameters for Sgr A*. Further calculations provide information about the model's variability compared to observations. Subsequently, we present results from the non-thermal radiation calculations at $2.2 \mu\text{m}$, including the resulting light curve, an analysis of flares, and a comparison with the GRMHD simulation results.

3.1. Radiation at 230 GHz

Observations of Sgr A* at 230 GHz have been conducted by various telescopes, including the Submillimeter Array (SMA), the Atacama Large Millimeter/submillimeter Array (ALMA), and notably, the Event Horizon Telescope (EHT). The latter, in particular, has provided a wealth of high-resolution images from the innermost region of the accretion disk onto Sgr A* itself, presenting an invaluable resource for the scientific community (EHT collaboration 2022a-f). Thus there exists a plethora of data on the properties of the lightcurve at that particular frequency. Therefore, utilizing much of this data, our main goals are to reproduce the main features of the light curve at 230 GHz (amplitude and variability) by calibrating the various physical parameters from dimensionless code units to actual physical units. When we combine how the flux changes with distance and angle (as illustrated in Fig. 4), it becomes clear that the majority of the radiation is emanating from a distance of approximately $10 r_g$. This underscores that the events we are studying occur in extremely close proximity to the black hole, and consequently, the critical data points we are interested in are highly concentrated in this area.

As we know from observations (Wielgus et al. 2022) the radiation flux of Sgr A* at 230 GHz is approximately stable. In order to turn the parameters of the GRMHD simulation from code units to physical cgs units a conversion and calibration of variables is necessary. We define a scaling parameter S , that appropriately multiplies physical quantities such as magnetic field (B), pressure (P) and density (ρ) to convert values of physical quantities from geometric (code) units to cgs units. Obviously, the conversion leaves unchanged dimensionless quantities such as Θ_e , σ , and β

$$B_{cgs} = \sqrt{4\pi} c S^{1/2} B_{geometric} \quad (23)$$

$$\rho_{cgs} = S \rho_{geometric} \quad (24)$$

$$P_{cgs} = c^2 S P_{geometric} \quad (25)$$

Through an iterative procedure applied in various snapshots of the GRMHD calculation, the model limited the radiation flux in

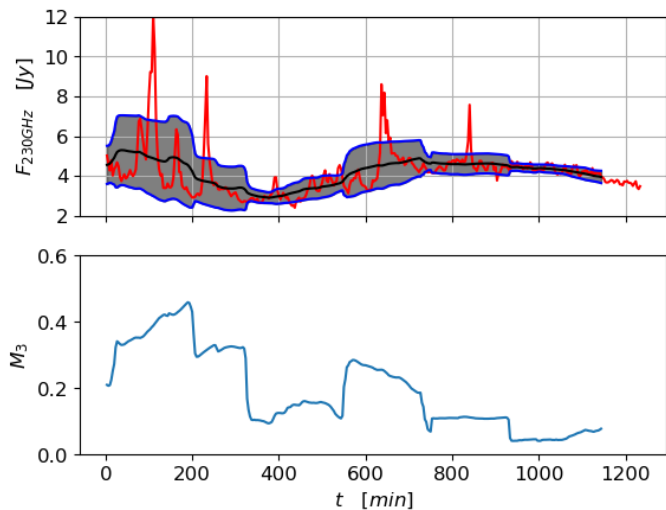


Fig. 5. Top panel: the lightcurve at 230 GHz (red line), the moving average of the lightcurve (m_3 , in a time window of 3 hours, black line) and the $1s_3$ standard deviation (grey area). Lower panel: The measure of variability the lightcurve M_3 defined as $M_3 = s_3/m_3$.

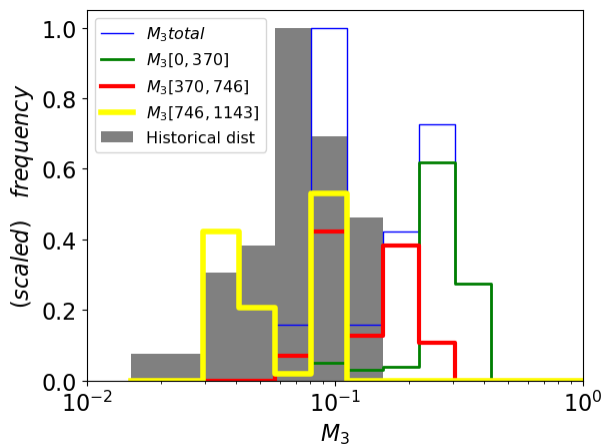


Fig. 6. Distribution of M_3 of the lightcurve at 230 GHz (blue) compared with historical data from observations of Sgr A* (grey). We have also cut the lightcurve and respectively M_3 in three time intervals, first for $t \in [0, 370]$ min (green), second for $t \in [370, 746]$ min (red) and third for $t \in [746, 1143]$ min (yellow).

a range around 4 Jy and finally produced the value of the scaling parameter S . After calculating the parameter S we can calculate the radiation flux at all snapshots and finally produce the lightcurve at 230 GHz. The upper panel of Fig. 5 presents the lightcurve at 230 GHz (red line). Noticeably, the radiation flux remains almost constant throughout the calculation period. The higher flux values observed in the beginning of the light curve gradually decrease towards the end of the evolution.

To investigate the variability of the lightcurve we define the moving average radiation flux over a 3-hour period (m_3 , black line in Fig. 5) and the standard deviation over the same duration (s_3 , grey area in Fig. 5). The lower panel of Fig. 5 shows the spread of M_3 where $M_3 = s_3/m_3$. M_3 is a measure of the variability of the lightcurve and can be compared with historical observations from Sgr A* (Fig. 6).

Sgr A* lightcurve shifts and changes over time due to a combination of stellar winds and turbulence on various scales. Longer changes come from variations in the stellar winds, espe-

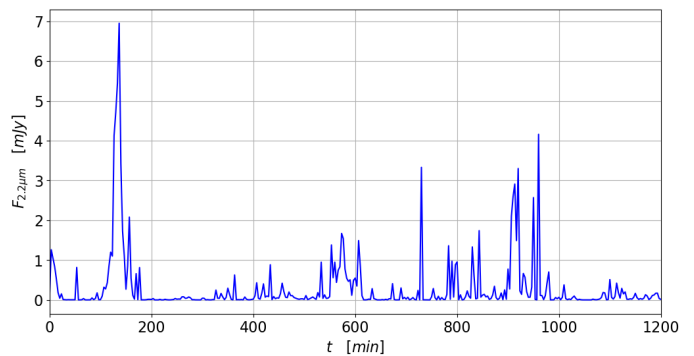


Fig. 7. Lightcurve at $2.2\mu\text{m}$. Our model can produce one very bright flare around 7 mJy and another three that pass the threshold of 1.5 mJy.

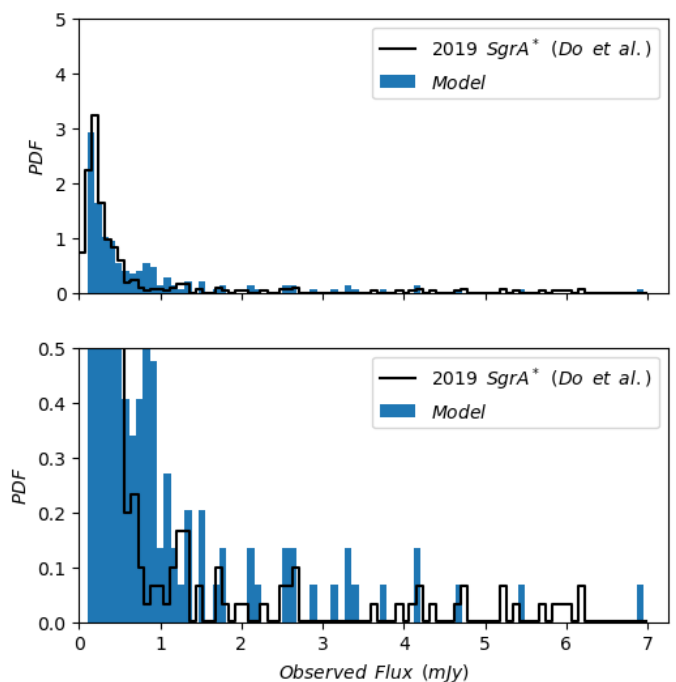


Fig. 8. Histogram comparison between our model and observations from Do et al. (2019).

cially near the S stars. Shorter changes happen because of turbulence closer to the center. The spread of M_3 in Fig. 5 exhibits a downward trend, suggesting that if we keep running the same simulation for further time, the flare variability will eventually stabilize at lower levels. Fig. 6 is a histogram of M_3 that provides a broader view derived from observing Sgr A*, the historical data is represented in gray (see Wielgus et al. 2022). The other distributions are derived from the simulation results for different time windows. It is important to keep in mind that the yellow line distribution represents the last part of the M_3 curve inside the time interval $t \in [746, 1143]$ min. This closely aligns with the observations and shows that a new calculation of the same model for longer times will probably yield the desired variability in the lightcurve.

3.2. Results at 2.2 μm (NIR flares)

3.2.1. Lightcurve and statistics

In Fig. 3 we carefully marked the specific areas where non-thermal radiation processes occur. These dynamic areas reside within the funnel region and in the limit of the disk. There is an environment characterized by high magnetization and low plasma β values which are important to activate the radiation mechanisms with sufficient efficiency. In Section 2.3 we discussed in detail that it is this local environment that characterises the process of acceleration for the plasma residing within current sheets.

Using data from these regions, we calculate the light curve at 2.2 μm , and our results are depicted in Fig. 7. Notably, during quiescent states, the average flux is remarkably low, consistent with observations. Within the simulation, several flares occur, each typically exceeding a flux of > 1.5 mJy (Witzel et al. 2021; von Fellenberg et al. 2023). Noteworthy, there are four flares during the simulation time that surpass this threshold, with an additional three flares marginally meeting the criteria for acceptance as flares. One particularly significant radiation flare, with a flux of approximately 7 mJy and a longer duration than typical flares, stands out as a potential candidate within the observed limits for both flux and duration, resembling to the unprecedented flare reported in Do et al. 2019.

In a theoretical comparison with observations we do not have a flux limit that allows us to define what is considered as flare and what not but it is obvious that the values of the flux in Fig. 7 rise up several orders of magnitude between a quiescent and a flare state ($F \gtrsim 1.5$ mJy). Sgr A* produces flares with lower flux but also some very bright ones ($F > 6$ mJy; Do et al. 2019) like those produced in our model. In Fig. 8 we see a comparison of the historical flux distribution in histogram for Sgr A* from Witzel et al. 2018 as presented in Do et al. (2019) compared to the high flux flare observed in 2019. The probability of observing such a flare (>6 mJy) was computed to be less than 0.05% (Witzel et al. 2018). Our model is capable of reproducing high-flux flares that cover the full range of observations.

According to Fig. 8 our model appears to have fairly good statistics in terms of the population of flares and in terms of their intensity. This is not the case for Sgr A* flares generated from MAD models which seem to show a very large population of flares and tend to overproduce the quiescent state flux (Dexter et al. 2020; Scepi et al. 2022; White & Quataert 2022). This is probably due to the very strong magnetic field they possess, and to the fact that the main source of the flares is the current sheet in the equator which feeds high values of absorptivity in the density due to the \dot{M} (as seen characteristically in the paper of Scepi et al. 2022).

Another crucial variable to consider is the cooling time of particles responsible for producing non-thermal radiation. Our method for computing the light curve involves each simulation snapshot radiating under the assumption of the fast cooling regime. Additionally, no cooling effects are considered, treating all radiation as if emitted instantaneously. The accuracy of this approach depends on the estimation of the cooling parameter. The cooling time of a particle with Lorentz factor γ due to synchrotron radiation is given by the equation:

$$t_{\text{syn}} = \frac{\gamma m_e c^2}{4/3 \sigma_T c U_B \gamma^2 \beta^2} \quad (26)$$

where the Lorentz factor γ is $\gamma = (v/v_L)^{1/2}$. Using typical values for magnetic field B from our model, approximately 60 G for the

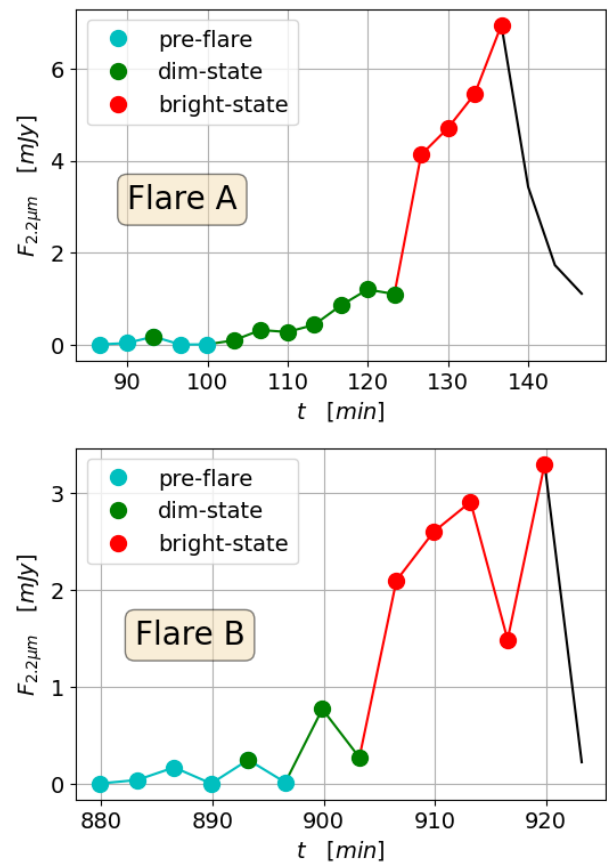


Fig. 9. Part of the lightcurve at 2.2 μm . In the upper plot, Flare A, for $t \in [86, 150]$ min (the first bright flare with approximately 7 mJy radiation flux) and in the bottom plot, Flare B, for $t \in [879, 926]$ min (a bright flare with two peaks). The duration of the flares is about 40-60 minutes, duration relevant to observations. We can divide the lightcurve in three states: pre-flare, dim-state and bright-state. This separation is based on the flux and spectral index

region of interest calculating the cooling time from relation (26) we obtain $t_{\text{syn}} \sim 3$ min. This suggests that particles have enough time to radiate their energy in a snapshot of the GRMHD simulation, given that simulation outputs occur every 10 M, which translates to approximately 200 seconds for Sgr A*. Therefore, cooling effects do not significantly impact the calculation.

3.2.2. Properties of flares

In the upper panel of Fig. 9 we zoom in on the first major flare within the time range $t \in [86, 150]$, hereafter referred to as Flare A. Whereas, on the lower panel, we zoom on a second, smaller flare within the time range $t \in [879, 926]$, hereafter referred to as Flare B. We examine how the properties of each flare change across three different stages: the pre-flare state, which occurs when the flux is several orders of magnitude smaller than 1 mJy; the dim-state, which occurs when the flux begins to increase (as shown in Fig. 11, where the spectral index also increases) and finally, the bright-state, which occurs when the flux exceeds 1 mJy. In both flares, we can see the specific points and their corresponding colors that represent the three different states. Each point is derived from a specific snapshot of the GRMHD simulation. The first flare is characterized by a distinct peak, while the second flare has two peaks. Similar phenomena have been observed (GRAVITY Collaboration et al. 2018). The classifica-

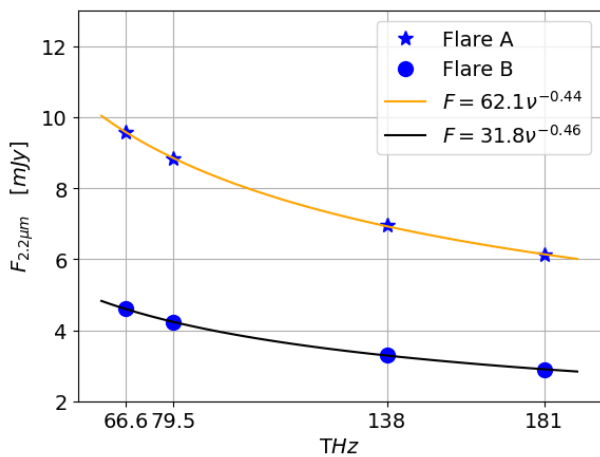


Fig. 10. Radiation flux around $2.2 \mu\text{m}$. Specific to the frequencies 66.6 (M- band), 79.5 (L-band), 138 (K-band) and 181 (H-band) THz for Flare A (stars) and Flare B (circles). The fitting (black and orange) lines correspond to power-laws where the exponential gives us the spectral index of the spectrum, in our case $a = -0.44$ for Flare A and $a = -0.46$ for Flare B.

tion of points into the different flare states was based on flux and spectral index. The rationale for this classification is clearly illustrated in Fig. 11.

Following the same calculation methods used for the non-thermal radiation, we estimate the radiation flux at three additional frequencies: 66.6, 79.5, and 181 THz, which correspond to the M, L, and H bands, respectively. The primary frequency of our calculation, $2.2 \mu\text{m}$ (138 THz), corresponds to the K-band for Sgr A*. For this calculation we used two snapshots at times $t = 136$ min and $t = 920$ min, one for each flare at the peak of the bright state. We thus extract the spectrum of our model for this flare state (Fig. 10). The fitting curves in Fig. 10 can give us the spectral index (which defined as the exponent of a power law like $F \propto \nu^a$) for each flare. The two values that we obtained ($a = -0.46$ and $a = -0.44$) are within the observed range (Ghez et al. 2005b,a; Bremer et al. 2011).

During a flare, both the flux and the spectral index simultaneously increase. We categorize the points into three groups, distinguished by the colors used to represent them. Fig. 11 shows the evolution of the spectral index as the flares transition from the pre-flare state to the dim-state and finally to the bright-state. The fitting power law curve (orange line) approximates how the spectral index evolves as the flare transitions from one state to the next, which is comparable to observations (Bremer et al. 2011). The same colors were used to distinguish the points in Fig. 9.

3.2.3. Flare states compared with GRMHD simulation

As a final property of the flares we wanted to see how these peaks in the lightcurve relate to the GRMHD calculation from which the phenomena originated. Therefore, we plotted the parameters ρ , σ and plasma β , which play crucial roles in determining the current sheet (Fig. 12). The plots refer to the three states of the second flare we investigated, specifically the snapshots at times $t = 886$ min (pre-flare), $t = 900$ min (dim-state), $t = 910$ min (bright-state). The corresponding points of these snapshots can be seen in the light curve of Fig. 9.

The plot of the density (ρ) (top row in Fig. 12) shows a clear structure in the upper funnel region that appears as the flare transitions from one state to the next. This structure is also character-

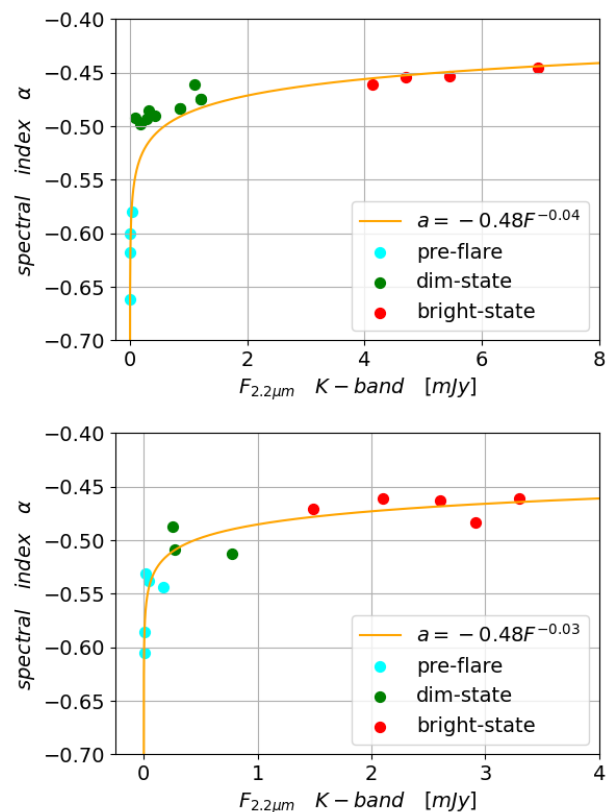


Fig. 11. Spectral index vs Flux for the two flares (Flare A upper plot and Flare B bottom plot). The dots correspond to the snapshots that are marked also in Fig. 9: cyan color corresponds to pre-flare states, green color represents the dim-state, red color represents the bright state of each flare. The orange lines are a fitting power-law curve which can be compared with observations

ized by low magnetization and high plasma β . According to the definition given above, it constitutes a clear current sheet which, in the bright-state, is surrounded by regions with high values of magnetization (σ) (middle row in Fig. 12) and low plasma β (bottom row in Fig. 12). These are ideal conditions for radiating non-thermal radiation. This current sheet in the bright state can be characterized as a plasmoid chain, similar to those seen in localized PIC simulations (Ball et al. 2018; Sironi & Spitkovsky 2014; Petropoulou & Sironi 2018).

It is important to emphasize that this increase in magnetization σ and decrease in plasma β in the bright state of the flares (conditions ideal for the activation of flares) are also found at the boundaries of the disk. These are possible regions for flare generation through high magnetic turbulence in the plasma, as mentioned in subsection 2.2. Fig. 12 clearly shows that the creation of the current sheet inside the funnel region is a phenomenon perfectly connected to the organization of the magnetic field and results in the creation of conditions (magnetization and plasma β) which will activate non-thermal particles in the current sheet itself and along the disk boundary.

Indeed, in accordance with the above, the areas that radiate are the current sheet and the disk boundary as shown in Fig. 13. Fig. 13 illustrates the radiation flux (in mJy), the slope p and the efficiency ϵ at time $t = 910$ min (bright state of Flare B that we investigate). The visible boxes in each plot correspond to the identification of current sheets and their environment as shown in Fig. 3. Within each box, all plasma quantities are averaged in order to characterize this specific reconnection region. However,

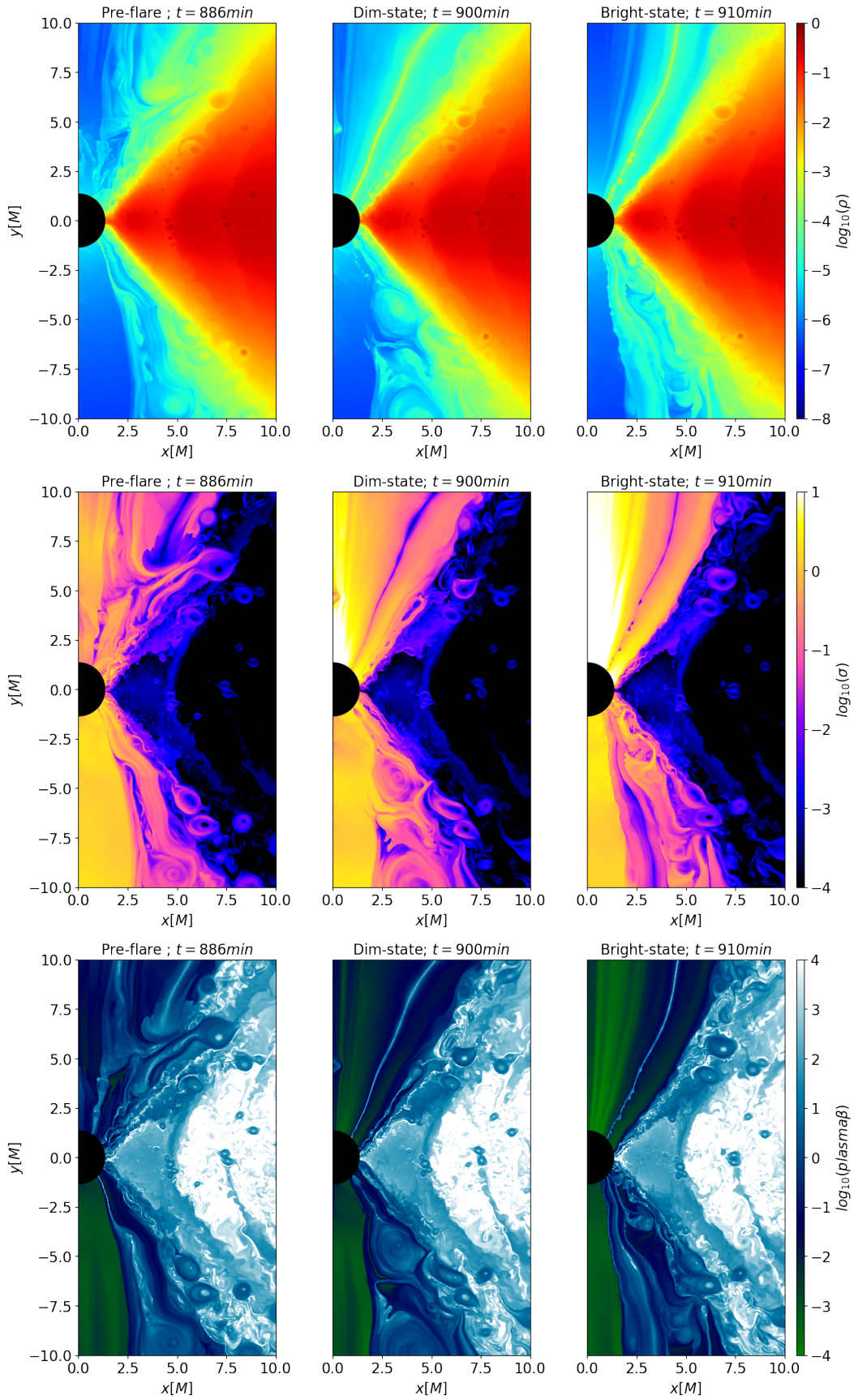


Fig. 12. Top row: density of the second bright flare ($t \in [886, 963]$ min) for its three states: pre-flare, dim-state, bright-state at snapshots $t = 886$ min, $t = 900$ min and $t = 910$ min respectively. Middle row: magnetization (σ) at the same snapshots. Bottom row: plasma β at the same snapshots. All panels refer to Flare B.

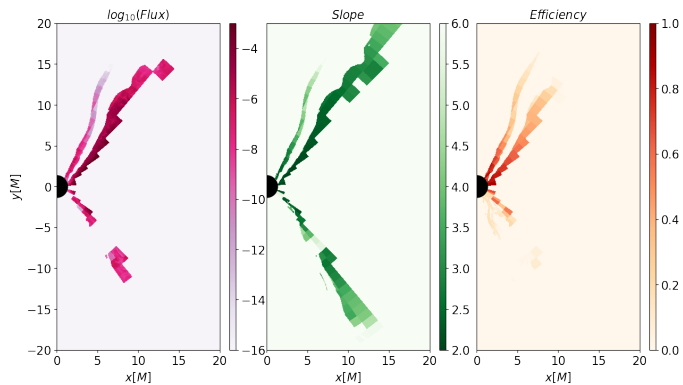


Fig. 13. Radiation flux at 2.2 microns (in mJy), slope p and efficiency ϵ in each grid point of the GRMHD simulation are shown in the left, middle and right panels, respectively. The plots illustrate the bright state of Flare B.

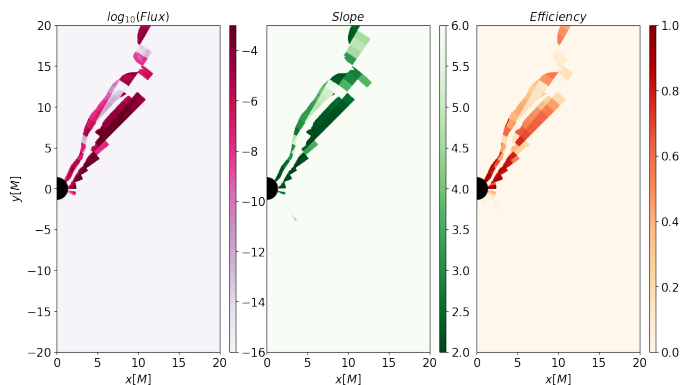


Fig. 14. Same plots as Fig. 13 but for the bright state of Flare A.

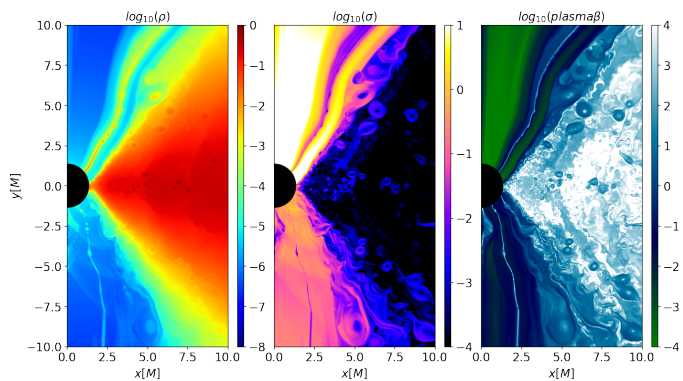


Fig. 15. Density (left panel), magnetization σ (middle panel) and plasma β (right panel) for Flare A in the bright state.

only the plasma within the current sheet layer - determined by the constraints and limits discussed in Section 2.3 - is considered to have the specific slope and efficiency, producing the reported flux. Two-thirds of the non-thermal radiation flux comes from the disc boundary, where the turbulent plasma dominates, while one-third comes from the current sheet.

Similar phenomena can be observed in Flare A at time $t = 136$ min. A clear current sheet has produced a plasmoid chain, and the local environment is characterised by high magnetization and low plasma β (see Fig. 15). Accordingly, the slope p and the efficiency ϵ (middle and right panel of Fig. 14) peak at the current sheet and produce the radiation flux (left panel of

Fig. 14), which strengthens our conclusions about how the flares are generated in this particular calculation.

4. Conclusions

We analyzed data from the GRMHD simulation of Nathanail et al. (2020), specifically focusing on model D, which is characterized as a SANE multi-loop model. Unlike MAD simulations, this model describes the accretion disk of a black hole without the production of a stable jet.

By applying a thermal radiation model to this particular simulation enabled us to reproduce the lightcurve at 230 GHz, from which we were able to calibrate the simulation variables. Encouragingly, the model's variability demonstrated good agreement with observations, prompting us to conduct larger simulations with extended time evolution.

In order to calculate the non-thermal radiation from the simulation, we introduced a novel method that identifies current sheets and places with high magnetic turbulence. This identification based on the magnetic field polarity reversals, is done by constraining primarily the current density together with the micro-physical plasma parameters, like magnetization and plasma β . After the identification is done, all quantities are averaged in the local environment. The constraints we placed on the parameters provided clear spatial boundaries within which to apply the model that calculates the non-thermal radiation. This association not only advances our comprehension of the fundamental processes at play, but also provides a crucial framework for future investigations in similar contexts.

The results for the lightcurve at 2.2 μm are very encouraging as they produce not only small flares up to 2 mJy but also a couple of brighter ones that reach 7 mJy. The duration of such flares is also consistent with observations. Further analysis of the flare spectral index demonstrated the success of the model in reproducing the observations. It is interesting that during the evolution of the flare the spectrum follows a power law similar to those given by the observations with spectral index $a = -0.44$.

In summary, we emphasize once again that a very important result of this work is the identification of the source of flaring non-thermal radiation in GRMHD simulations. We have clearly shown that such flares most probably originate in current sheets and their associated plasmoid chains in the funnel area, as well as in the disk boundary due to magnetic turbulence.

Acknowledgements

ID is supported by the Hellenic Foundation for Research and Innovation (HFRI) under the 4th Call for HFRI PhD Fellowships (Fellowship Number: 9239). Support comes from the ERC Advanced Grant "JETSET: Launching, propagation and emission of relativistic jets from binary mergers and across mass scales" (Grant No. 884631). CMF is supported by the DFG research grant "Jet physics on horizon scales and beyond" (Grant No. 443220636) within the DFG research unit "Relativistic Jets in Active Galaxies" (FOR 5195). This work was supported by computational time granted from the National Infrastructures for Research and Technology S.A. (GRNET S.A.) in the National HPC facility - ARIS - . Simulations were performed also on the GOETHE-HLR cluster at CSC in Frankfurt

Data Availability

The data underlying this article will be shared on reasonable request to the corresponding author.

References

- Aimar, N., Dmytriiev, A., Vincent, F. H., et al. 2023, *A&A*, 672, A62
- Antonopoulou, E. & Nathanail, A. 2024, arXiv e-prints, arXiv:2405.10115
- Ball, D., Özel, F., Christian, P., Chan, C.-K., & Psaltis, D. 2021, *ApJ*, 917, 8
- Ball, D., Sironi, L., & Özel, F. 2018, *The Astrophysical Journal*, 862, 80
- Bauböck, M., Dexter, J., Abuter, R., et al. 2020, *Astronomy & Astrophysics*, 635, A143
- Boehle, A., Ghez, A., Schödel, R., et al. 2016, *The Astrophysical Journal*, 830, 17
- Bremer, M., Witzel, G., Eckart, A., et al. 2011, *Astronomy & Astrophysics*, 532, A26
- Chatterjee, K., Markoff, S., Neilsen, J., et al. 2021, *Monthly Notices of the Royal Astronomical Society*, 507, 5281
- Comisso, L. & Sironi, L. 2019, *The Astrophysical Journal*, 886, 122
- Cruz-Orsorio, A., Fromm, C. M., Mizuno, Y., et al. 2022, *Nature Astronomy*, 6, 103
- Dahlin, J., Drake, J., & Swisdak, M. 2014, *Physics of Plasmas*, 21
- Davelaar, J., Olivares, H., Porth, O., et al. 2019, *A&A*, 632, A2
- Del Zanna, L., Zanotti, O., Bucciantini, N., & Londrillo, P. 2007, *Astronomy & Astrophysics*, 473, 11
- Dexter, J., Tchekhovskoy, A., Jiménez-Rosales, A., et al. 2020, *Monthly Notices of the Royal Astronomical Society*, 497, 4999
- Dihingia, I. K., Mizuno, Y., Fromm, C. M., & Rezzolla, L. 2023a, *Monthly Notices of the Royal Astronomical Society*, 518, 405
- Dihingia, I. K., Mizuno, Y., Fromm, C. M., & Younsi, Z. 2023b, arXiv preprint arXiv:2305.09698
- Do, T., Witzel, G., Gautam, A. K., et al. 2019, *The Astrophysical Journal Letters*, 882, L27
- Dodds-Eden, K., Porquet, D., Trap, G., et al. 2009, *The Astrophysical Journal*, 698, 676
- Drake, J., Swisdak, M., & Fermo, R. 2012, *The Astrophysical Journal Letters*, 763, L5
- Eckart, A., García-Marín, M., Vogel, S., et al. 2012, *Astronomy & Astrophysics*, 537, A52
- EHT collaboration. 2022, *The Astrophysical Journal Letters*, 930, L12
- Fishbone, L. G. & Moncrief, V. 1976, *The Astrophysical Journal*, 207, 962
- Fromm, C. M., Cruz-Orsorio, A., Mizuno, Y., et al. 2022, *A&A*, 660, A107
- Genzel, R., Eisenhauer, F., & Gillessen, S. 2010, *Reviews of Modern Physics*, 82, 3121
- Ghez, A., Hornstein, S., Lu, J., et al. 2005a, *The Astrophysical Journal*, 635, 1087
- Ghez, A., Salim, S., Hornstein, S. D., et al. 2005b, *The Astrophysical Journal*, 620, 744
- Ghisellini, G. 2013, *Radiative processes in high energy astrophysics*, Vol. 873 (Springer)
- GRAVITY Collaboration, Abuter, R., Amorim, A., et al. 2018, *A&A*, 618, L10
- GRAVITY Collaboration, Broderick, A. E. & Loeb, A. 2005, *Monthly Notices of the Royal Astronomical Society*, 363, 353
- GRAVITY Collaboration, Abuter, R., Aimar, N., Amorim, A., et al. 2022, *Astronomy & Astrophysics*, 657, L12
- GRAVITY Collaboration, Abuter, R., Amorim, A., Anugu, N., et al. 2018, *Astronomy & Astrophysics*, 615, L15
- Guo, F., Li, H., Daughton, W., & Liu, Y.-H. 2014, *Physical Review Letters*, 113, 155005
- Guo, F., Liu, Y.-H., Daughton, W., & Li, H. 2015, *The Astrophysical Journal*, 806, 167
- Jiang, H.-X., Mizuno, Y., Dihingia, I. K., et al. 2024, arXiv e-prints, arXiv:2404.03237
- Jiang, H.-X., Mizuno, Y., Fromm, C. M., & Nathanail, A. 2023, *MNRAS*, 522, 2307
- Leung, P. K., Gammie, C. F., & Noble, S. C. 2011, *The Astrophysical Journal*, 737, 21
- Li, X., Guo, F., Li, H., & Li, G. 2015, *The Astrophysical Journal Letters*, 811, L24
- Li, X., Guo, F., Liu, Y.-H., & Li, H. 2023, *ApJ*, 954, L37
- Lin, X., Li, Y.-P., & Yuan, F. 2023, *MNRAS*, 520, 1271
- Lin, X. & Yuan, F. 2024, arXiv e-prints, arXiv:2405.17408
- Matsumoto, T., Chan, C.-H., & Piran, T. 2020, *Monthly Notices of the Royal Astronomical Society*, 497, 2385
- Mellah, I. E., Cerutti, B., & Crinquand, B. 2023, arXiv preprint arXiv:2305.01689
- Meringolo, C., Cruz-Orsorio, A., Rezzolla, L., & Servidio, S. 2023, *The Astrophysical Journal*, 944, 122
- Mościbrodzka, M., Falcke, H., & Shiokawa, H. 2016, *Astronomy & Astrophysics*, 586, A38
- Nathanail, A., Dhang, P., & Fromm, C. M. 2022, *Monthly Notices of the Royal Astronomical Society*, 513, 5204
- Nathanail, A., Fromm, C. M., Porth, O., et al. 2020, *MNRAS*, 495, 1549
- Nathanail, A., Mpisketzi, V., Porth, O., Fromm, C. M., & Rezzolla, L. 2022, *MNRAS*, 513, 4267
- Olivares, H., Porth, O., Davelaar, J., et al. 2019, *Astronomy & Astrophysics*, 629, A61
- Pandya, A., Zhang, Z., Chandra, M., & Gammie, C. F. 2016, *The Astrophysical Journal*, 822, 34
- Petropoulou, M. & Sironi, L. 2018, *Monthly Notices of the Royal Astronomical Society*, 481, 5687
- Petropoulou, M., Sironi, L., Spitkovsky, A., & Giannios, D. 2019, *ApJ*, 880, 37
- Ponti, G., George, E., Scaringi, S., et al. 2017, *Monthly Notices of the Royal Astronomical Society*, 468, 2447
- Porth, O., Chatterjee, K., Narayan, R., et al. 2019, *ApJSS*, 243, 26
- Porth, O., Mizuno, Y., Younsi, Z., & Fromm, C. 2021, *Monthly Notices of the Royal Astronomical Society*, 502, 2023
- Porth, O., Olivares, H., Mizuno, Y., et al. 2017, *MNRAS*, 4, 1
- Ripperda, B., Liska, M., Chatterjee, K., et al. 2022, *The Astrophysical Journal Letters*, 924, L32
- Rybicki, G. B. & Lightman, A. P. 1986, *Radiative Processes in Astrophysics*
- Scepi, N., Dexter, J., & Begelman, M. C. 2022, *Monthly Notices of the Royal Astronomical Society*, 511, 3536
- Shay, M., Haggerty, C., Phan, T., et al. 2014, *Physics of Plasmas*, 21
- Sironi, L. & Spitkovsky, A. 2014, *The Astrophysical Journal Letters*, 783, L21
- Čemeljić, M., Yang, H., Yuan, F., & Shang, H. 2022, *ApJ*, 933, 55
- Viergutz, S. 1993, *Astronomy and Astrophysics*, Vol. 272, p. 355 (1993), 272, 355
- von Fellenberg, S. D., Witzel, G., Bauböck, M., et al. 2023, *A&A*, 669, L17
- Vos, J. T., Olivares, H., Cerutti, B., & Mościbrodzka, M. 2024, *MNRAS*[arXiv:2309.03267]
- Werner, G. R., Uzdensky, D. A., Begelman, M. C., Cerutti, B., & Nalewajko, K. 2018, *Monthly Notices of the Royal Astronomical Society*, 473, 4840
- White, C. J. & Quataert, E. 2022, *ApJ*, 926, 136
- Wielgus, M., Marchili, N., Martí-Vidal, I., et al. 2022, *The Astrophysical Journal Letters*, 930, L19
- Witzel, G., Martínez, G., Hora, J., et al. 2018, *ApJ*, 863, 15
- Witzel, G., Martínez, G., Willner, S. P., et al. 2021, *ApJ*, 917, 73
- Younsi, Z. & Wu, K. 2015, *Monthly Notices of the Royal Astronomical Society*, 454, 3283
- Zhang, H., Sironi, L., Giannios, D., & Petropoulou, M. 2023, *ApJ*, 956, L36